


Emergence of cubic ordered full-plane persistent spin textures in lead-free materials

Sajjan Sheoran ^{*}, Preeti Bhumla , and Saswata Bhattacharya [†]

Department of Physics, Indian Institute of Technology Delhi, New Delhi 110016, India

 (Received 18 June 2022; revised 15 August 2022; accepted 23 August 2022; published 6 September 2022)

The materials preserving a uniform spin configuration in the momentum space, known as persistent spin texture (PST), provide long carrier spin lifetimes through persistent spin-helix mechanism. However, most of the PSTs studied until now are attributed to the linear in \mathbf{k} splitting and cease to exist locally around certain high-symmetry points of the first Brillouin zone (BZ). The PSTs with purely cubic spin splittings (PCS) have drawn attention owing to unique benefits in spin transport. Here, using relativistic first-principles calculations supplemented with $\mathbf{k} \cdot \mathbf{p}$ analysis, we report the emergence of PCS belonging to D_{3h} point group, which is enforced by in-plane mirror and threefold rotation operations. In addition, the in-plane mirror symmetry operation sustains the PST in a larger region, i.e., full planes of BZ alongside giant spin splitting. The observed PSTs provide a route to nondephasing spin transport with larger spin Hall conductivity, thereby offering a promising platform for future spintronics devices.

DOI: [10.1103/PhysRevMaterials.6.094602](https://doi.org/10.1103/PhysRevMaterials.6.094602)

I. INTRODUCTION

In nonmagnetic solids, one can naively expect the electron energy bands having up and down spins to be degenerate in absence of a magnetic field. However, in systems that break spatial inversion symmetry, spin-orbit coupling (SOC) generates a momentum- (\mathbf{k} -) dependent spin-orbit field (SOF), $\Omega(\mathbf{k}) \propto \mathbf{E} \times \mathbf{k}$, where \mathbf{E} is the electric field induced by the inversion asymmetry of the crystal [1–5]. The SOF lifts the spin band degeneracy, resulting in nontrivial \mathbf{k} -dependent spin textures mainly through Rashba and Dresselhaus effects [6–11]. The charges with opposite spin have opposite directions in momentum space. Thus, they show spin-selective transport. In particular, linear Rashba (LR) effect has attracted much attention since it can electrically manipulate the spin degrees of freedom and produce nonequilibrium spin polarization [12–14]. These phenomena are steering a new way in various intriguing fields, including spintronics and topological matter [15–19].

The momentum-dependent spin splittings are well explained by linear Rashba (LR), linear Dresselhaus (LD), or some unique combination of LR and LD [9–14,20,21]. In linear spin splitting including LR or LD, energy levels are dispersed with crystal momentum (\mathbf{k}) having the relation $E_{\mathbf{k}} = \alpha \mathbf{k}^2 \pm \tau \mathbf{k}$, where α and τ are the effective mass and linear splitting terms, respectively. The LR and LD can be described by SOC perturbed Hamiltonians $H_{LR} = \alpha_R(\sigma_x k_y - \sigma_y k_x)$ and $H_{LD} = \alpha_D(\sigma_x k_x - \sigma_y k_y)$, respectively [10]. Here, α_R and α_D are the constants signifying the strength of LR and LD effects, respectively, and σ_i ($i = x, y, z$) are the Pauli matrices. However, the SOF arising from LR or LD will introduce two kinds of spin dephasing mechanisms, viz., Elliott-Yafet spin

relaxation and Dyakonov-Perel spin dephasing, limiting the experimental realization of spin currents. The persistent spin texture (PST), where spin configurations become independent of the (\mathbf{k}), enables a route to overcome spin dephasing and provides nondissipative spin transport [16,20–24]. In the regime of linear splitting, PST can be obtained by tuning the strength of LR and LD effects, such that they compensate each other ($\alpha_R = \alpha_D$). In addition, PST with linear spin splitting can also be enforced by nonsymmorphic space-group symmetry of the crystal and, therefore, not easily broken [20]. In recent times, cubic Rashba (CR) and cubic Dresselhaus (CD) effects have started to gain scrutiny owing to their unique benefits to spin transport like larger spin Hall conductivity as compared to linear spin-splitting effects [3,4,6,25–28]. The purely cubic effects (CR or CD) can be distinguished from linear effects (LR or LD) by dispersion curve $E_{\mathbf{k}} = \alpha \mathbf{k}^2 \pm \eta \mathbf{k}^3$ [see Fig. 1(a)]. The CR and CD effects are described by the SOC Hamiltonians given by $H_{CR} = (k_x - ik_y)^3(\sigma_x + i\sigma_y) - (k_x + ik_y)^3(\sigma_x - i\sigma_y)$ and $H_{CD} = (k_x k_z^2 - k_y k_z^2)\sigma_x + (k_y k_x^2 - k_z k_y^2)\sigma_y + (k_z k_x^2 - k_z k_y^2)\sigma_z$, respectively. The crucial experimental discoveries related to CR contain SrTiO₃(001) surface [4], asymmetric oxide heterostructure LaAlO₃/SrTiO₃/LaAlO₃ [26], strained-Ge/SiGe quantum well [3], and surfaces of antiferromagnets GdIr₂Si₂ and TbRh₂Si₂ [29,30].

Recently, symmetry-enforced purely cubic splitting (PCS) was predicted for bulk materials by deriving the two-band xaps $\mathbf{k} \cdot \mathbf{p}$ model of all 21 polar point-group symmetries, having C_{3h} , D_{3h} , and T_d ($\bar{6}$, $\bar{6}m2$, and $43m$ in Hermann-Mauguin notation) as the associated point-group symmetries [31]. However, splitting in T_d point group corresponds to trivial CD, which can be seen in zinc-blende-type crystal structures [32]. In addition, it was also shown that the crystals with C_{3h} and D_{3h} point-group symmetries show PST with PCS around the Γ point [see Fig. 1(b)]. These types of PSTs are preserved by the symmetry and, thus, are robust to spin-independent impurities and do not easily get destroyed.

^{*}phz198687@physics.iitd.ac.in

[†]saswata@physics.iitd.ac.in

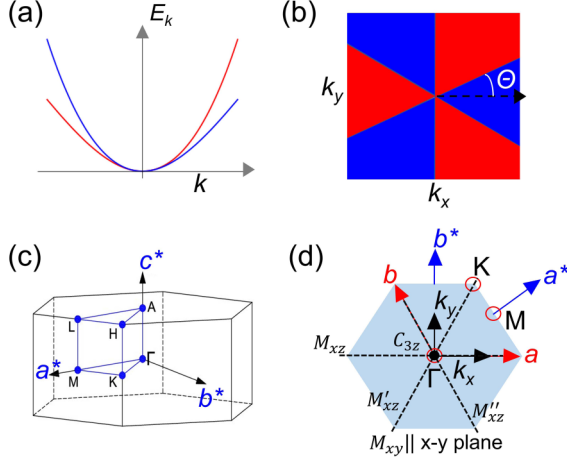


FIG. 1. (a) Schematic illustration of band structure due to purely cubic spin splitting. Here, the band energies E_k vary with k in the form $E_k = \alpha k^2 \pm \eta k^3$. (b) Schematic PST due to cubic spin splittings. The color represents the out-of-plane (z) component of spin textures [note that in-plane (x -, y -) spin components are zero]. Here, the red and blue colors denote the spins in the state $|\uparrow\rangle$ and $|\downarrow\rangle$, respectively. Here, $|\uparrow\rangle$ and $|\downarrow\rangle$ are the eigenstates of σ_z with eigenvalues $+1$ and -1 , respectively. Θ is the angular difference between line separating the sectors with eigenvalues $+1$ and -1 , and $k_x = 0$. (c) First BZ of the hexagonal structure. Blue lines highlight the path used for band structure calculation. (d) BZ of the hexagonal structure within the $(k_x$ - k_y) plane, where k_x and k_y are the Cartesian reciprocal lattice vectors. The lattice vectors are denoted by a and b , whereas the reciprocal ones are represented by a^* and b^* , respectively. The symmetry elements (C_{3z} , M_{xy} , and M_{xz}) of the D_{3h} point group are also shown. The black solid dotted and dashed lines represent the rotation axis and mirror planes, respectively.

These findings are reported for $\text{Ge}_3\text{Pb}_5\text{O}_{11}$, $\text{Pb}_7\text{Br}_2\text{F}_{12}$, and $\text{Pb}_7\text{Cl}_2\text{F}_{12}$ having $P\bar{6}$ space-group symmetry (with C_{3h} associated point-group symmetry) [31]. However, $\text{Ge}_3\text{Pb}_5\text{O}_{11}$ is only stable at temperatures above 450 K, and conduction band minima (CBM) of $\text{Pb}_7\text{Br}_2\text{F}_{12}$ and $\text{Pb}_7\text{Cl}_2\text{F}_{12}$ do not lie in the vicinity of the Γ point [31,33]. Alongside these limitations, the presence of toxic element Pb is also a concern. Therefore, finding novel materials which can circumvent these limitations is essential.

In this work, using state-of-the-art first-principles-based density-functional-theory (DFT) calculations, duly supplemented with the effective model Hamiltonian derived from the $\mathbf{k} \cdot \mathbf{p}$ invariant method, we reveal the emergence of PCS in a large family of materials with D_{3h} point-group symmetry. We find that the in-plane mirror and threefold rotation symmetry of the crystal lead to the PCS around Γ and A points in the BZ. In addition, the PSTs are observed in a larger region and preserved in whole Γ - M - K plane [see Figs. 1(c) and 1(d) for the plane]. More importantly, $\text{K}_3\text{Ta}_3\text{B}_2\text{O}_{12}$ exhibits giant spin splitting, which is particularly observed around the Γ , M , and A points in the proximity of the CBM. Our calculations also show that magnitude of the spin splitting can be tuned with the application of uniaxial strain preserving the full-plane PST.

II. COMPUTATIONAL METHODS

We have employed the relativistic first-principles calculations based on density-functional theory (DFT) as implemented in Vienna *ab initio* simulation package (VASP) [34,35]. The simulations are done using plane-wave basis set and projector augmented wave method [36,37]. We have used the Perdew-Burke-Ernzerhof revised for solids (PBEsol) as the exchange-correlation (ϵ_{xc}) functional [38] and set plane-wave cutoff energy to 550 eV. To get a more accurate band gap, calculations are also performed using nonlocal Heyd-Scuseria-Ernzerhof (HSE06) ϵ_{xc} functional [39]. Initially, experimental lattice parameters and atomic positions are taken as a starting point. In structural optimization, the change in total energy between two electronic steps is set to 10^{-6} eV and are converged until Hellmann-Feynman forces are smaller than $1 \text{ meV } \text{\AA}^{-1}$ without including spin-orbit coupling. The Brillouin zone was sampled in \mathbf{k} space with Monkhorst-Pack [40] scheme with a k mesh of $6 \times 6 \times 12$ for $\text{K}_3\text{Ta}_3\text{B}_2\text{O}_{12}$ and KTaGe_3O_9 and $8 \times 8 \times 6$ for $\text{Sr}_7\text{Br}_2\text{H}_{12}$. After the structure optimization, we have also confirmed the dynamical stability using density-functional perturbation theory (DFPT). The phonon dispersion curves are calculated by considering $2 \times 2 \times 2$ supercell with the PHONOPY code [41]. The spin textures from DFT are calculated using a dense \mathbf{k} mesh of 51×51 around high-symmetry point in k_x - k_y plane. The model band structures and spin textures are calculated by parametrizing the models using minimization of the summation

$$S = \sum_{i=1}^2 \sum_{\mathbf{k}} f(\mathbf{k}) |\text{Det}[H(\mathbf{k}) - E^i(\mathbf{k})I]|^2 \quad (1)$$

over i th energy eigenvalues $[E^i(\mathbf{k})]$ as training sets, where $f(\mathbf{k})$ is the weight attached to \mathbf{k} point. Here, H , “Det,” and I represent model Hamiltonian, determinant, and identity matrix, respectively. We have used normal distribution for $f(\mathbf{k})$ to get a better fit near high-symmetry point as used in Refs. [31,42]. We have conducted symmetry analysis using Ref. [43], Bilbao crystallographic server [44,45], SEEK-PATH software [46], and FINDSYM [47]. The *Mathematica* [48] and PYPROCAR [49] are used to plot spin textures, band structures, and parametrize the models. Since considered materials are nonmagnetic, we have not artificially initialized spin configurations; the final spin configurations are determined by VASP after fully converging the electronic self-consistent loop. For considering the strain, we have varied the lattice parameter (c) with respect to equilibrium lattice parameter (c_0) and further relaxed the atomic coordinates.

III. SYMMETRY ANALYSIS AND ELECTRONIC BAND STRUCTURES

We have screened lead-free experimentally synthesized nonmagnetic materials having band gap greater than 1.0 eV with space groups $P\bar{6}$, $P\bar{6}m2$, $P\bar{6}2m$, $P\bar{6}2c$, and $P\bar{6}c2$, from AFLOW [50] and Materials Project [51] data repositories. There is rather a large family of materials which crystallize in these space groups, and can show PST with PCS [see Sec. I of Supplemental Material (SM) [52]]. In particular, we are interested in materials, which are dynamically stable,

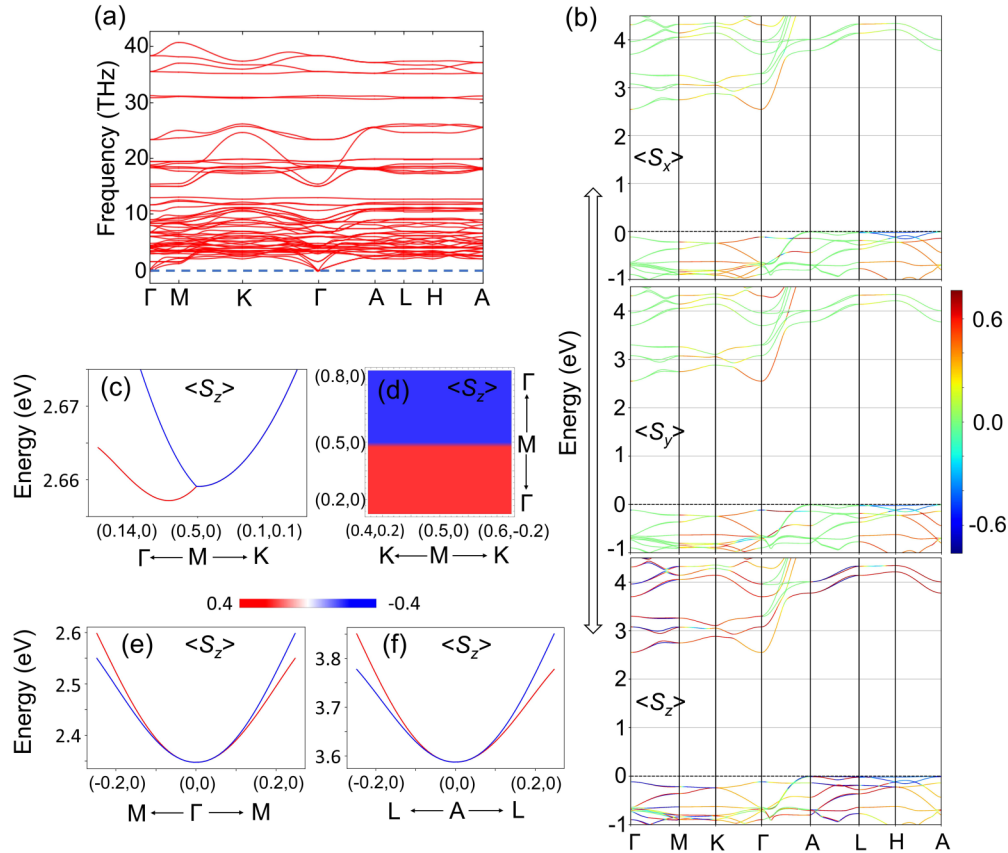


FIG. 2. (a) Calculated phonon dispersion for $\text{K}_3\text{Ta}_3\text{B}_2\text{O}_{12}$. (b) Spin-resolved band structures along high-symmetry path are shown. The color bars represent the expectation values of the S_x , S_y , and S_z spin components. (c) The calculated spin-resolved band structure of lower conduction bands along the path K - M - Γ . (d) Spin texture of lower conduction band around the M point in $k_z = 0$ plane. Note that there should be two spin textures associated with two bands. Here, the only one branch associated with the outer band is shown. The inner branch has an opposite spin orientation with respect to outer branch at every (k_x, k_y) point. The spin-resolved band structures around (e) Γ point (along M - Γ - M) and (f) A point (along L - A - L). The k point (k_x, k_y) ranges considered to compute the band structure and spin textures around the high-symmetry point are indicated in the units of reciprocal lattice vectors $(\frac{2\pi}{|a|}, \frac{2\pi}{|b|})$, where a and b are the real lattice vectors.

have suitable band edge positions, wide band gap, and exhibit giant splitting. Therefore, we have particularly focused on $\text{K}_3\text{Ta}_3\text{B}_2\text{O}_{12}$ ($P62m$), KTaGe_3O_9 ($P6c2$) with D_{3h} point-group symmetry, and $\text{Sr}_7\text{Br}_2\text{H}_{12}$ ($P6$) with C_{3h} point-group symmetry. The symmetry elements of D_{3h} point group are shown in Fig. 1(d). The threefold rotation axis along z direction (C_{3z}), the vertical mirror plane containing the x axis (M_{xz}), and the horizontal mirror plane perpendicular to the z axis (M_{xy}) generate the D_{3h} point group. The C_{3h} point group is subgroup of D_{3h} and contains C_{3z} and M_{xy} as symmetry elements. The relaxed crystal structures and atomic positions are shown in Sec. II of SM [52]. Our relaxed crystal structures are in good agreement with the experimentally synthesized crystal structures. The calculated lattice parameters (a , c) deviate from experimental ones [53–55] by (1.2%, 1.2%), (0.3%, 2.1%), and (1.5%, 1.4%) for $\text{K}_3\text{Ta}_3\text{B}_2\text{O}_{12}$, KTaGe_3O_9 , and $\text{Sr}_7\text{Br}_2\text{H}_{12}$, respectively. Subsequently, the dynamical stability of these materials is tested by analyzing their phonon spectra. Figure 2(a) shows the phonon spectrum for $\text{K}_3\text{Ta}_3\text{B}_2\text{O}_{12}$ along the high-symmetry path given in Fig. 1(c) (see Sec. III of SM [52] for phonon plots of KTaGe_3O_9 and $\text{Sr}_7\text{Br}_2\text{H}_{12}$). The absence of negative frequencies in the phonon dispersion plots

confirms the dynamical stability of these structures at low temperature.

After that, we have calculated the band structures using PBEsol ϵ_{xc} functional with inclusion of SOC. Figure 2(b) shows spin-projected band structures of $\text{K}_3\text{Ta}_3\text{B}_2\text{O}_{12}$. A band gap of 2.51 eV is calculated with CBM and valence band maximum (VBM) at Γ and A points, respectively. Since PBEsol is known to underestimate the band gap, we have also calculated the band gap using more sophisticated hybrid ϵ_{xc} functional HSE06. The obtained band gap using HSE06 ϵ_{xc} functional is 4.01 eV. Similarly we have also calculated band gaps of KTaGe_3O_9 and $\text{Sr}_7\text{Br}_2\text{H}_{12}$ (see Sec. IV of SM [52]). The HSE06 band gaps come out to be 4.74 and 4.84 eV for KTaGe_3O_9 and $\text{Sr}_7\text{Br}_2\text{H}_{12}$, respectively.

IV. SPIN SPLITTING AND EFFECTIVE k - p HAMILTONIAN

Inclusion of SOC leads to splitting of bands throughout the BZ. In $\text{K}_3\text{Ta}_3\text{B}_2\text{O}_{12}$, splitting is predominantly present for lower conduction band along Γ - M , A - L directions [see in Fig. 2(b)] and nearly absent for upper valence band. This is due to the fact that lower conduction band mainly

TABLE I. The transformations of $(\sigma_x, \sigma_y, \sigma_z)$ and (k_x, k_y, k_z) with respect to the generators of the C_{2v} , D_{3h} , and C_{3h} point group and time-reversal operator (T). The first row shows the point-group operations and the corresponding point-group symmetries. Note that the generators are enough to form the whole group. Hence, only these generators along with time-reversal $T = i\sigma_y K$ operation (K is complex-conjugation operator) are considered to construct the $\mathbf{k} \cdot \mathbf{p}$ model. The last row shows the terms which are invariant under point-group operation. Note that we have included the terms up to cubic in \mathbf{k} and higher-order contributions are found to be insignificant.

| Operations | $C_{3z} = e^{-i\pi/3\sigma_z}$ (D_{3h}, C_{3h}) | $M_{xz} = i\sigma_y$ (D_{3h}, C_{2v}) | $M_{xy} = i\sigma_z$ (D_{3h}, C_{3h}, C_{2v}) | $T = i\sigma_y K$ |
|------------|---|--|--|--|
| k_x | $-k_x/2 + \sqrt{3}k_y/2$ | k_x | k_x | $-k_x$ |
| k_y | $-\sqrt{3}k_x/2 - k_y/2$ | $-k_y$ | k_y | $-k_y$ |
| k_z | k_z | k_z | $-k_z$ | $-k_z$ |
| σ_x | $-\sigma_x/2 + \sqrt{3}\sigma_y/2$ | $-\sigma_x$ | $-\sigma_x$ | $-\sigma_x$ |
| σ_y | $-\sqrt{3}\sigma_x/2 - \sigma_y/2$ | σ_y | $-\sigma_y$ | $-\sigma_y$ |
| σ_z | σ_z | $-\sigma_z$ | σ_z | $-\sigma_z$ |
| Invariants | $(k_x\sigma_y - k_y\sigma_x),$ $k_y(3k_x^2 - k_y^2)\sigma_z,$ $k_x(k_x^2 - 3k_y^2)\sigma_z$ | $k_i^m k_j \sigma_x, k_i^m k_j \sigma_z,$ $k_i^m k_x \sigma_y, k_i^m k_z \sigma_y$ ($i = x, y, z; m = 0, 2$) | $k_i^m k_x \sigma_z, k_i^m k_y \sigma_z,$ $k_i^m k_z \sigma_x, k_i^m k_z \sigma_y$ ($i = x, y, z; m = 0, 2$) | $k_i \sigma_j$ ($i, j = x, y, z$) |

consists of heavier Ta-5d orbitals, whereas O-2p orbitals contribute to upper valence band. Along the path Γ -M-K- Γ ($k_z = 0$ plane), it is clearly seen that the band dispersion is entirely characterized by the out-of-plane spin component. On the contrary, the in-plane spin component is almost absent along that path. The observed PST is different from the widely reported PST, which occurs locally around high-symmetry points or along lines of first BZ. The in-plane mirror symmetry of crystal (M_{xy}) enforces spin components to hold the relation $(S_x, S_y, S_z) \rightarrow (-S_x, -S_y, S_z)$, which satisfies only when in-plane components are zero. This leads to out-of-plane SOF, which is considered to be the z axis. Figures 2(c) and 2(d) show the conduction bands and associated spin textures around the M point, respectively. The spin-split bands are predominantly linear in \mathbf{k} . For deeper insights, the band dispersion can be deduced by identifying all the symmetry-allowed terms such that $H(\mathbf{k}) = O^\dagger H(\mathbf{k})O$, where O is symmetry operations belonging to the group of wave vector (G) associated with the high-symmetry point and time-reversal symmetry (T) [56]. The invariant Hamiltonian should satisfy the condition given below,

$$H_G(\mathbf{k}) = D(O)H(O^{-1}\mathbf{k})D^{-1}(O), \quad \forall O \in G, T \quad (2)$$

where $D(O)$ is the matrix representation of operation O belonging to point group G . The $\mathbf{k} \cdot \mathbf{p}$ Hamiltonian is derived using the method of invariants by considering the little group of M point to be C_{2v} , consisting of mirror planes M_{xz} and M_{xy} besides identity operation (E). The $\mathbf{k} \cdot \mathbf{p}$ Hamiltonian around the M point, following the transformation rules listed in Table I, is given by [10]

$$H_{C_{2v}}(\mathbf{k}) = H_0(\mathbf{k}) + \gamma k_y \sigma_z + \delta k_z \sigma_y, \quad (3)$$

where $H_0(\mathbf{k})$ is the part of Hamiltonian describing the band dispersion, depending on the parameters α and β as

$$H_0(\mathbf{k}) = E_0 + \alpha k_x^2 + \beta k_y^2, \quad (4)$$

α and β are related to the effective masses (m_x^* , m_y^*) by the expressions $|\alpha| = \frac{\hbar^2}{2m_x^*}$ and $|\beta| = \frac{\hbar^2}{2m_y^*}$, respectively. σ are the Pauli matrices describing spin degrees of freedom. γ and δ are the linear SOC splitting coefficients. For dispersion relation in

(k_x - k_y) plane around M point, Eq. (3) takes the form

$$H_{C_{2v}}(\mathbf{k}) = H_0(\mathbf{k}) + \gamma k_y \sigma_z. \quad (5)$$

The eigenstates corresponding to Eq. (5) are given by

$$\Psi_{\mathbf{k}\uparrow} = e^{i\mathbf{k}\cdot\mathbf{r}} \begin{pmatrix} 1 \\ 0 \end{pmatrix} \quad (6)$$

and

$$\Psi_{\mathbf{k}\downarrow} = e^{i\mathbf{k}\cdot\mathbf{r}} \begin{pmatrix} 0 \\ 1 \end{pmatrix}. \quad (7)$$

The corresponding eigenvalues are given as

$$E_{C_{2v}}^\pm(\mathbf{k}) = E_0 + \alpha k_x^2 + \beta k_y^2 \pm \gamma k_y. \quad (8)$$

The spin textures determined by the expression $S_\pm = \frac{\hbar}{2} \langle \Psi_{\mathbf{k}\uparrow, \downarrow} | \sigma | \Psi_{\mathbf{k}\uparrow, \downarrow} \rangle$ are given as

$$S_\pm = \pm \frac{\hbar}{2} (0, 0, 1). \quad (9)$$

Equation (9) shows that only out-of-plane spin component is present around the M point and is found to be consistent with DFT spin texture shown in Fig. 2(d). By fitting the DFT band structure and spin texture around the M point, we find that $\gamma = 3.11$ eV Å. This splitting is significantly larger as compared to other bulk systems such as BiTeCl ($\alpha_R = 1.2$ eV Å) [57], BiAlO₃ ($\alpha_R = 0.74$ eV Å) [13], and LaWN₃ ($\alpha_R = 2.7$ eV Å) [19,42].

Figure 2(e) shows the splitting around Γ point. The spin-split bands around Γ are purely cubic in \mathbf{k} with only the z component being nonvanishing [see Fig. 2(b)]. The splittings around the Γ points can be understood in terms of effective $\mathbf{k} \cdot \mathbf{p}$ Hamiltonian. Here, the group of the wave vector associated with the Γ point remains the D_{3h} , comprising of trivial identity operation (E), C_{3z} , and four mirror planes (M_{xy} , M_{xz} , M'_{xz} , and M''_{xz}). The Hamiltonian for the (k_x - k_y) plane taking into account the symmetry invariants up to cubic in \mathbf{k} (see Table I) can be expressed as

$$H_{D_{3h}}(\mathbf{k}) = H_0(\mathbf{k}) + \lambda k_y (3k_x^2 - k_y^2) \sigma_z, \quad (10)$$

where λ is the cubic SOC splitting coefficient. The eigenstates corresponding to this Hamiltonian are $\Psi_{\mathbf{k}\downarrow}$ and $\Psi_{\mathbf{k}\uparrow}$. The

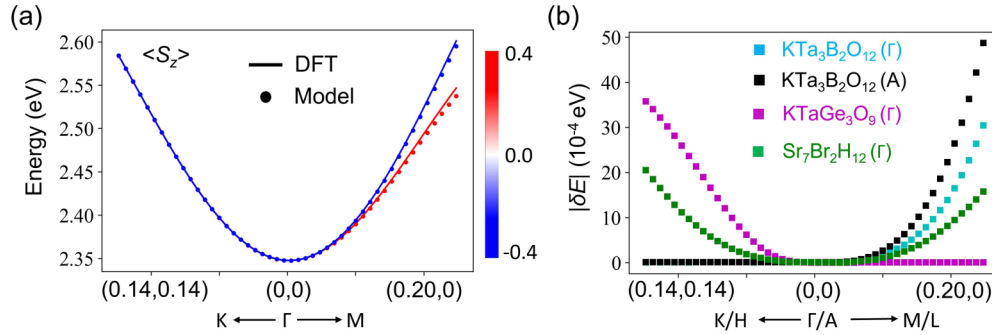


FIG. 3. (a) Conduction bands of $K_3Ta_3B_2O_{12}$ around the Γ point projected over z component of spin direction. (b) Spin-splitting energies (δE) of $K_3Ta_3B_2O_{12}$ (CBM), $KTaGe_3O_9$ (VBM), and $Sr_7Br_2H_{12}$ (VBM). Band structure and δE are plotted along $(\frac{2\pi}{a}0.14, \frac{2\pi}{b}0.14)-(0,0)-(\frac{2\pi}{a}0.14, 0)$ direction of the momentum space, which is along $K(H)-\Gamma(A)-K(M)$ direction. The magnitude of δE is defined as $|\delta E| = |E(k, \uparrow) - E(k, \downarrow)|$, where $E(k, \uparrow)$ and $E(k, \downarrow)$ are the energy bands with up and down spins, respectively.

cubic-split eigenvalues of Eq. (10) are obtained as

$$E_{D_{3h}}^{\pm}(\mathbf{k}) = E_0 + \alpha k_x^2 + \beta k_y^2 \pm 3\lambda k_x^2 k_y \mp \lambda k_x^3. \quad (11)$$

The expectation values for the spin operators are the same as given by Eq. (9), confirming the unidirectional spin texture around the Γ point. Note that the Hamiltonian given by Eq. (10) depends upon the choice of coordinate system and is valid only for space groups $P\bar{6}2m$ and $P\bar{6}2c$. The symmetry-allowed term for D_{3h} point group associated with $P\bar{6}m2$ and $P\bar{6}c2$ is $\zeta k_x(k_x^2 - 3k_y^2)\sigma_z$ instead of $\lambda k_y(3k_x^2 - k_y^2)\sigma_z$. This is particularly due to the fact that mirror operation present in $P\bar{6}m2$ and $P\bar{6}c2$ is M_{yz} instead of M_{xz} (see the detailed discussion in Sec. V of SM [52]). Additionally, $P\bar{6}$ space group is linked to the C_{3h} point group and at the Γ point, the little group remains C_{3h} . The effective two-band Hamiltonian following the transformation rules given in Table I, up to the third order in \mathbf{k} in the (k_x-k_y) plane, is given by [31]

$$H_{C_{3h}}(\mathbf{k}) = H_0(\mathbf{k}) + \zeta k_x(k_x^2 - 3k_y^2)\sigma_z + \lambda k_y(3k_x^2 - k_y^2)\sigma_z \quad (12)$$

and the corresponding energy eigenvalues with eigenstates ($\Psi_{\mathbf{k}\uparrow}$, $\Psi_{\mathbf{k}\downarrow}$) are

$$E_{C_{3h}}^{\pm}(\mathbf{k}) = E_0 + \alpha k_x^2 + \beta k_y^2 \pm \zeta k_x^3 \pm 3\lambda k_x^2 k_y \mp 3\zeta k_y^2 k_x \mp \lambda k_y^3. \quad (13)$$

The additional cubic splitting term with coefficient ζ arises for the C_{3h} point group because the symmetry is reduced as compared to the D_{3h} point group. The Bloch states $\Psi_{\mathbf{k}\uparrow}$ and $\Psi_{\mathbf{k}\downarrow}$ are the eigenstates of σ_z leading to zero in-plane spin polarization around the Γ and M points. Only the out-of-plane spin polarization is nonvanishing, leaving to PST over full Γ - M - K plane in $P\bar{6}$, $P\bar{6}m2$, $P\bar{6}2m$, $P\bar{6}2c$, and $P\bar{6}c2$ space-group materials. The splitting observed around M and Γ points is linear and cubic in nature, respectively. The $\mathbf{k} \cdot \mathbf{p}$ model and DFT give the same nature of spin splitting and textures. It is also worth emphasizing that the above two-band models are also applicable to the other \mathbf{k} points, whose little group is identical to the Γ or M points. In $P\bar{6}$, $P\bar{6}m2$, $P\bar{6}2m$, $P\bar{6}2c$, and $P\bar{6}c2$ space groups, the little group of A and L points are same as for Γ and M points, respectively. Here, the PST over entire L - A - H high-symmetry path with PCS is also observed [see Figs. 2(b) and 2(f)].

We have compared the band structures and spin textures of $K_3Ta_3B_2O_{12}$ around the Γ point with HSE06, PBE, PBEsol, and PBE+ U (here, U is the Hubbard parameter) ϵ_{xc} functionals to validate the choice of functional. The value of U is taken to be 2.5 eV to include the onsite Coulomb repulsion energy for Ta-5d orbitals, in accordance with previous studies [58]. It is found that all the spin-splitting properties except band gap calculated with HSE06, PBE, PBE+ U are within $\pm 5\%$ as compared to PBEsol (see Sec. VI of SM [52]). Therefore, our calculations are based on computationally efficient PBEsol ϵ_{xc} functional. First, we have calculated the band structure for the split bands along k_x and k_y directions. Then, we have fitted the band structure to $\mathbf{k} \cdot \mathbf{p}$ model and the results are shown in Fig. 3(a) for $K_3Ta_3B_2O_{12}$. Our model fits the DFT band structure very well. The observed splitting is found to be highly anisotropic and depends upon the space-group symmetry of the material. The bands are spin split along Γ - M direction and degenerate along the Γ - K direction. Anisotropic effective mass could lead to the anisotropic splitting, but, in our case, the effective mass is observed to be isotropic in both the Γ - K and Γ - M directions. To further analyze the anisotropy, we have plotted the magnitude of the energy difference ($|\delta E| = |E(k, \uparrow) - E(k, \downarrow)|$) between the split bands [see Fig. 3(b)]. The splitting is completely absent in the Γ - K and A - H directions for $K_3Ta_3B_2O_{12}$ and Γ - M direction for $KTaGe_3O_9$. The splitting for $Sr_7Br_2H_{12}$ is present along both Γ - M and Γ - K directions with different magnitudes. The different contributions coming from the terms with splitting coefficients ζ and λ lead to anisotropic splitting along Γ - M and Γ - K directions.

Furthermore, the spin textures around the Γ and A points for the considered systems are also obtained using DFT and $\mathbf{k} \cdot \mathbf{p}$ models. Figures 4(a) and 4(b) are the obtained spin textures of $K_3Ta_3B_2O_{12}$ around the Γ point. The spin textures are momentum (\mathbf{k}) independent with nonzero out-of-plane components with a mere in-plane component around the Γ point in $K_3Ta_3B_2O_{12}$. Figures 4(c) and 4(d) show the spin textures calculated using $\mathbf{k} \cdot \mathbf{p}$ model and are in accordance with the DFT results. It is interesting to note that the spin textures of considered configurations are different from each other. The border lines separating the $+|s_z|$ and $-|s_z|$ sectors vary with materials under consideration. To understand this, the spin-projected constant energy contours of inner and outer bands are computed as shown in Fig. 4(e). Here, spin projected

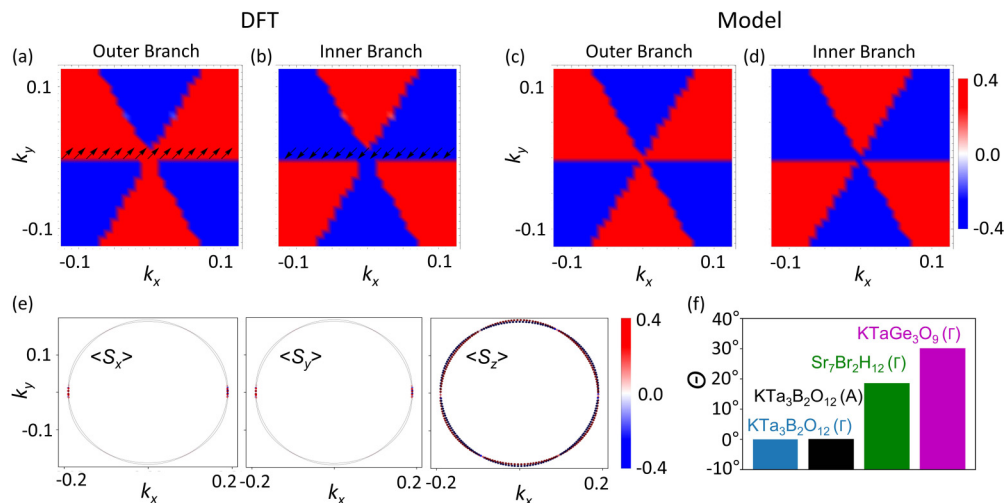


FIG. 4. Spin textures of the conduction bands for $K_3Ta_3B_2O_{12}$ around the Γ point obtained by DFT [(a) and (b)] and $\mathbf{k} \cdot \mathbf{p}$ model [(c) and (d)]. Our spin textures are prepared using the convention [(a)–(d) as examples] that the energy of the outer branch is smaller or equal as compared to the energy of inner branch at any (k_x, k_y) point in the considered range. The arrows and color represent the in-plane (x, y) and out-of-plane (z) components of spin textures, respectively. (e) Constant energy contours projected over the spin components having energy of $E_F + 2.38$ eV. Here, the red and blue dots denote the spins in the states $|\uparrow\rangle$ and $|\downarrow\rangle$, respectively. (f) The calculated values of Θ for spin textures of $K_3Ta_3B_2O_{12}$, $KTaGe_3O_9$, and $Sr_7Br_2H_{12}$.

means expectation values of spin operators are computed for each \mathbf{k} point on constant energy contours. In fact, the border lines are the directions along which the energies of two bands with opposite spins become equal [see Fig. 4(e)]. We have

$$\tan(\Theta) = \begin{cases} -\frac{\xi}{\lambda} - \frac{(\xi^2 + \lambda^2)^{2/3}}{\lambda(\xi + i|\lambda|)^{1/3}} - \frac{(\xi^2 + \lambda^2)^{1/3}(\xi + i|\lambda|)^{1/3}}{\lambda} \\ -\frac{\xi}{\lambda} + \frac{(1 - i\sqrt{3})(\xi^2 + \lambda^2)^{1/3}(\xi + i|\lambda|)^{1/3}}{2\lambda} + \frac{(1 + i\sqrt{3})(\xi^2 + \lambda^2)^{2/3}}{2\lambda(\xi + i|\lambda|)^{1/3}} \\ -\frac{\xi}{\lambda} + \frac{(1 + i\sqrt{3})(\xi^2 + \lambda^2)^{1/3}(\xi + i|\lambda|)^{1/3}}{2\lambda} + \frac{(1 - i\sqrt{3})(\xi^2 + \lambda^2)^{2/3}}{2\lambda(\xi + i|\lambda|)^{1/3}} \end{cases}. \quad (14)$$

Figure 4(f) shows Θ for the considered configurations. It is found to be consistent with DFT results (see Sec. VII of SM [52]). The angular difference between any two border lines of spin textures is calculated to be 60° , leading to the threefold rotation symmetry, which is in line with the threefold rotation symmetry of the crystal. Our calculations show that there is rather a big class of materials that support PST with PCS. All of these materials along with the calculated parameters are reported in Table II. Table II also includes the already reported parameters of $Ge_3Pb_5O_{11}$, $Pb_7Cl_2F_{12}$, and $Pb_7Br_2F_{12}$ for comparison. The splitting observed around the Γ point for $K_3Ta_3B_2O_{12}$ ($\lambda = 6.85$ eV \AA^3) is larger as compared to $Ge_3Pb_5O_{11}$ ($\chi = -5.24$ eV \AA^3), $Pb_7Br_2F_{12}$ ($\lambda = -5.04$ eV \AA^3), and comparable to $Pb_7Cl_2F_{12}$ ($\lambda = 8.65$ eV \AA^3). The splitting in $K_3Ta_3B_2O_{12}$ around the A point is $\lambda = 8.13$ eV \AA^3 , larger than that around the Γ point. Note that the orbital's contribution determines whether the PSTs with significant splitting occurs in the VB or CB. Giant splitting occurs when the heavy-atom orbitals contribute for the splitting bands. For example, splitting of VB is nearly absent as compared to CB in $K_3Ta_3B_2O_{12}$ since the mostly O-2p contribute for VB. The magnitude of splitting in these materials can be further increased by doping heavier elements with large SOC [59] and introducing strain [15,60] to make its experimental detec-

tion more easily accessible (i.e., spin-resolved photoemission spectroscopy).

V. EFFECTS OF STRAIN

Strain can affect the band structure of semiconductors by tuning their band gaps, varying effective mass of carriers, shifting bands, and introducing new band splitting [56]. Tuning of bands gaps, variation in effective mass of carriers, and shifting of bands are general consequences of strain. However, new band splittings are observed when the symmetry of a crystal changes with the application of strain [61]. The effect of the strain is extensively studied for LR and LD effects [15,60,62–66], however, it is still not explored for PCS. Here, we have introduced the out-of-plane strain such that the point-group symmetry of crystal remains intact. We have varied the strain from -5% to 5% , where “ $-$ ” and “ $+$ ” denote the compressive and tensile strain, respectively. In case of materials with D_{3h} point group, the border lines separating the $+|s_z|$ and $-|s_z|$ sectors (Θ) remain same. The PSTs including border line directions are robust to the strain and are protected by the symmetry. The splitting coefficients for $K_3Ta_3B_2O_{12}$ and $KTaGe_3O_9$ are tuned with the application of strain. Figures 5(a)–5(f) show the split bands and corresponding spin

TABLE II. The materials showing PCS with PST along with their parameters of Eq. (12). The splitting is observed for lower conduction bands (CB) or higher valence bands (VB) around the high-symmetry points (HSP) Γ and A.

| Materials | CB/VB | HSP | E_0 (eV) | α (eV \AA^2) | ζ (eV \AA^3) | λ (eV \AA^3) | Ref. |
|---|-------|----------|------------|-------------------------------|------------------------------|--------------------------------|-----------|
| BaHfSi ₃ O ₉ | VB | Γ | -0.19 | 3.05 | 0.65 | 0.00 | |
| BiTa ₇ O ₁₉ | VB | Γ | 0.00 | -3.79 | 2.35 | 0.00 | |
| BiTa ₇ O ₁₉ | CB | Γ | 2.82 | -1.20 | 0.55 | 0.00 | |
| LaTa ₇ O ₁₉ | VB | Γ | -0.19 | -3.28 | 0.95 | 0.00 | |
| LaTa ₇ O ₁₉ | CB | Γ | 3.56 | -1.23 | 9.55 | 0.00 | |
| KCaP ₃ O ₉ | VB | Γ | -0.15 | 1.96 | 0.85 | 0.00 | |
| KMgP ₃ O ₉ | VB | Γ | -0.19 | 2.13 | 1.00 | 0.00 | |
| KTaGe ₃ O ₉ | VB | Γ | -0.35 | 1.44 | 8.05 | 0.00 | |
| RbNbGe ₃ O ₉ | VB | Γ | -0.11 | 1.26 | 4.30 | 0.00 | |
| TlTaGe ₃ O ₉ | VB | Γ | -0.15 | 1.59 | 6.35 | 0.00 | |
| TlTaGe ₃ O ₉ | CB | Γ | 3.58 | 1.86 | 1.52 | 0.00 | This work |
| K ₃ Ta ₃ B ₂ O ₁₂ | CB | Γ | 2.34 | 5.04 | 0.00 | 6.85 | |
| K ₃ Ta ₃ B ₂ O ₁₂ | CB | A | 5.37 | 5.05 | 0.00 | 8.13 | |
| K ₄ Au ₆ S ₅ | VB | Γ | 0.00 | -0.95 | 0.00 | 5.55 | |
| K ₄ Au ₆ S ₅ | CB | Γ | 1.62 | 8.07 | 0.00 | 2.01 | |
| RbS | VB | Γ | 0.00 | -0.91 | 0.00 | 1.06 | |
| W ₆ CCl ₁₈ | CB | Γ | 1.04 | 0.51 | 0.00 | 9.10 | |
| Sr ₇ Cl ₂ H ₁₂ | VB | Γ | 0.00 | -1.13 | 2.35 | 1.80 | |
| Sr ₇ Br ₂ H ₁₂ | VB | Γ | 0.00 | -1.07 | 3.21 | 2.45 | |
| Pb ₇ Br ₂ F ₁₂ | CB | A | 3.43 | -3.11 | -0.91 | -4.36 | |
| Pb ₇ Cl ₂ F ₁₂ | CB | A | 3.63 | 5.11 | 1.23 | 8.18 | |
| Pb ₇ Br ₂ F ₁₂ | CB | Γ | 3.76 | -1.11 | -2.92 | -5.04 | |
| Pb ₇ Cl ₂ F ₁₂ | CB | Γ | 3.98 | -2.08 | 1.75 | 8.65 | [31] |
| Ge ₃ Pb ₅ O ₁₁ | CB | Γ | 2.13 | 1.27 | -5.24 | -3.43 | |

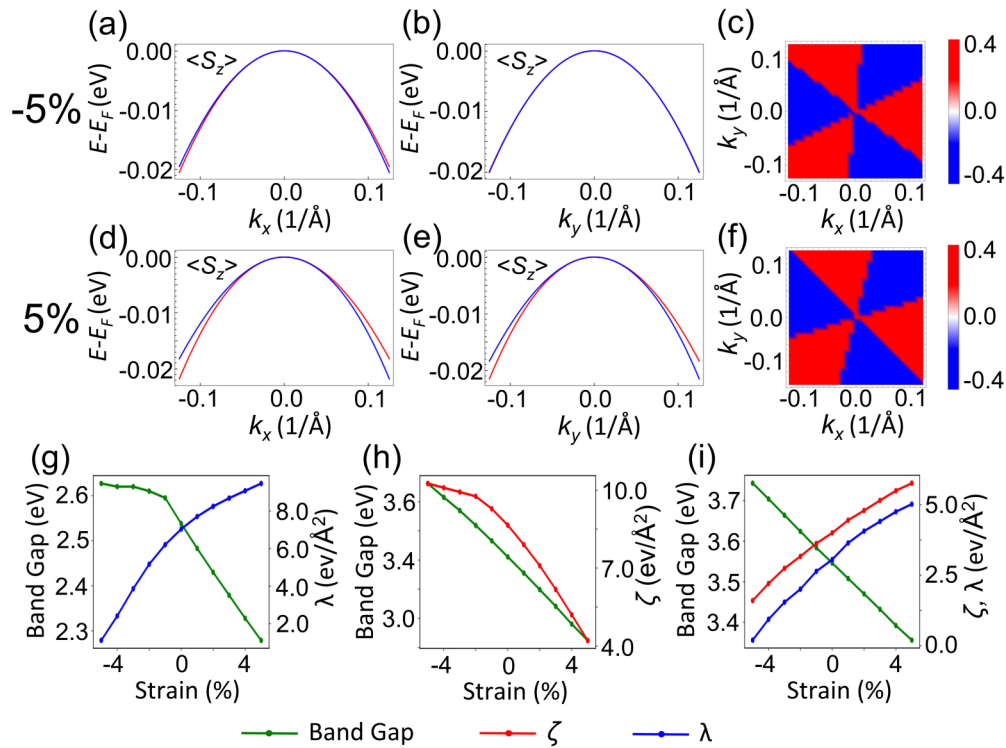


FIG. 5. Band structures and spin texture of the valence bands for Sr₇Br₂H₁₂ around the the Γ point under -5% [(a)–(c)] and 5% [(d)–(f)] strain obtained by DFT. Note that there should be two spin-texture branches associated to two bands; only one branch (associated with outer band) is shown for each case. The variation in band gap and splitting parameters (ζ and λ) as a function of strain for (g) K₃Ta₃B₂O₁₂, (h) KTaGe₃O₉, and (i) Sr₇Br₂H₁₂.

textures under the $\pm 5\%$ strain for $\text{Sr}_7\text{Br}_2\text{H}_{12}$. On the other hand, the spin splitting as well as spin textures are tuned for $\text{Sr}_7\text{Br}_2\text{H}_{12}$. The phonon spectrum shows that $\text{Sr}_7\text{Br}_2\text{H}_{12}$ is dynamically stable under such strain (see Sec. VIII of SM). The splitting increases (decreases) under tensile (compressive) strain. Figures 5(g)–5(i) show the variation of band gaps and splitting coefficients for $\text{K}_3\text{Ta}_3\text{B}_2\text{O}_{12}$, KTaGe_3O_9 , and $\text{Sr}_7\text{Br}_2\text{H}_{12}$ and are sensitive to strain. The observed linear trend is the same as for most of the linear splitting. In case of $\text{K}_3\text{Ta}_3\text{B}_2\text{O}_{12}$, the splitting can be increased from 6.85 eV \AA^3 (without any strain) to 9.45 eV \AA^3 at $+5\%$ strain [see Fig. 5(g)].

VI. CONCLUSIONS

Combining first-principles calculations and symmetry analysis, we have shown the existence of PST in bulk materials having D_{3h} and C_{3h} point-group symmetries. The unidirectional out-of-plane spin textures are observed in full Γ - M - K plane, as long as in-plane mirror symmetry remains intact and differs from trivial PST. In-plane mirror symmetry along with the threefold rotation symmetry leads to purely cubic spin splitting. Taking $\text{K}_3\text{Ta}_3\text{B}_2\text{O}_{12}$ as a test case, we have observed purely cubic splitting around the Γ point of an order $\approx 6.85 \text{ eV \AA}^3$, which is larger than the already reported

splitting. Around the M point, bands are linearly split with an order of $\approx 3.11 \text{ eV \AA}$. The observed splitting is found to be anisotropic in nature. The nature and anisotropy of splitting are also studied using the $\mathbf{k} \cdot \mathbf{p}$ model via symmetry analysis. Our calculations show that there exists a large family of materials which possess full-plane PST in purely cubical regime. In addition, strain engineering tunes the observed PST by varying the magnitudes of SOC splitting coefficients. These spin textures known for nondissipative spin transport, together with PCS, form another prospective aspect. The large SOC splitting coefficients, wide band gap, suitable band-edge positions, strain tunability, and room-temperature stability make them suitable for room-temperature applications. The complete realization of original device of these applications may enrich the field of spintronics.

ACKNOWLEDGMENTS

S.S. acknowledges CSIR, India, for the senior research fellowship [Grant No. 09/086(1432)/2019-EMR-I]. P.B. acknowledges UGC, India, for the senior research fellowship [Grant No. 1392/(CSIR-UGC-NET JUNE 2018)]. S.B. acknowledges financial support from SERB under a core research grant (Grant No. CRG/2019/000647) to set up his High Performance Computing (HPC) facility “Veena” at IIT Delhi for computational resources.

-
- [1] G. Dresselhaus, *Phys. Rev.* **100**, 580 (1955).
 [2] Y. A. Bychkov and E. I. Rashba, *JETP Lett.* **39**, 78 (1984); F. T. Vas'ko, *Pis'ma Zh. Eksp. Teor. Fiz.* **30**, 574 (1979); Y. A. Bychkov and E. I. Rashba, *ibid.* **39**, 66 (1984).
 [3] R. Moriya, K. Sawano, Y. Hoshi, S. Masubuchi, Y. Shiraki, A. Wild, C. Neumann, G. Abstreiter, D. Bougeard, T. Koga *et al.*, *Phys. Rev. Lett.* **113**, 086601 (2014).
 [4] H. Nakamura, T. Koga, and T. Kimura, *Phys. Rev. Lett.* **108**, 206601 (2012).
 [5] D. Xiao, G.-B. Liu, W. Feng, X. Xu, and W. Yao, *Phys. Rev. Lett.* **108**, 196802 (2012).
 [6] M. Gmitra and J. Fabian, *Phys. Rev. B* **94**, 165202 (2016).
 [7] D. Marchenko, A. Varykhalov, M. Scholz, G. Bihlmayer, E. Rashba, A. Rybkin, A. Shikin, and O. Rader, *Nat. Commun.* **3**, 1232 (2012).
 [8] S. D. Stranks and P. Plochocka, *Nat. Mater.* **17**, 381 (2018).
 [9] G. Bihlmayer, O. Rader, and R. Winkler, *New J. Phys.* **17**, 050202 (2015).
 [10] L. L. Tao, T. R. Paudel, A. A. Kovalev, and E. Y. Tsymbal, *Phys. Rev. B* **95**, 245141 (2017).
 [11] D. Di Sante, P. Barone, R. Bertacco, and S. Picozzi, *Adv. Mater.* **25**, 509 (2013).
 [12] S. Picozzi, *Front. Phys.* **2**, 10 (2014).
 [13] L. G. D. da Silveira, P. Barone, and S. Picozzi, *Phys. Rev. B* **93**, 245159 (2016).
 [14] J. Varignon, J. Santamaria, and M. Bibes, *Phys. Rev. Lett.* **122**, 116401 (2019).
 [15] R. Arras, J. Gosteau, H. J. Zhao, C. Paillard, Y. Yang, and L. Bellaiche, *Phys. Rev. B* **100**, 174415 (2019).
 [16] C. Autieri, P. Barone, J. Sławińska, and S. Picozzi, *Phys. Rev. Materials* **3**, 084416 (2019).
 [17] A. Stroppa, D. Di Sante, P. Barone, M. Bokdam, G. Kresse, C. Franchini, M.-H. Whangbo, and S. Picozzi, *Nat. Commun.* **5**, 5900 (2014).
 [18] K. Ishizaka, M. Bahramy, H. Murakawa, M. Sakano, T. Shimojima, T. Sonobe, K. Koizumi, S. Shin, H. Miyahara, A. Kimura *et al.*, *Nat. Mater.* **10**, 521 (2011).
 [19] S. Bandyopadhyay, A. Paul, and I. Dasgupta, *Phys. Rev. B* **101**, 014109 (2020).
 [20] L. Tao and E. Y. Tsymbal, *Nat. Commun.* **9**, 1 (2018).
 [21] H. Djani, A. C. Garcia-Castro, W.-Y. Tong, P. Barone, E. Bousquet, S. Picozzi, and P. Ghosez, *npj Quantum Mater.* **4**, 51 (2019).
 [22] F. Jia, S. Hu, S. Xu, H. Gao, G. Zhao, P. Barone, A. Stroppa, and W. Ren, *J. Phys. Chem. Lett.* **11**, 5177 (2020).
 [23] J. Schliemann, J. C. Egues, and D. Loss, *Phys. Rev. Lett.* **90**, 146801 (2003).
 [24] J. Schliemann, *Rev. Mod. Phys.* **89**, 011001 (2017).
 [25] K. V. Shanavas, *Phys. Rev. B* **93**, 045108 (2016).
 [26] W. Lin, L. Li, F. Doğan, C. Li, H. Rotella, X. Yu, B. Zhang, Y. Li, W. S. Lew, S. Wang *et al.*, *Nat. Commun.* **10**, 1 (2019).
 [27] D. C. Marinescu, *Phys. Rev. B* **96**, 115109 (2017).
 [28] J. Schliemann and D. Loss, *Phys. Rev. B* **71**, 085308 (2005).
 [29] S. Schulz, A. Y. Vyazovskaya, G. Poelchen, A. Generalov, M. Guttler, M. Mende, S. Danzenbacher, M. M. Otrokov, T. Balasubramanian, C. Polley, E. V. Chulkov, C. Laubschat, M. Peters, K. Kliemt, C. Krellner, D. Y. Usachov, and D. V. Vyalikh, *Phys. Rev. B* **103**, 035123 (2021).
 [30] D. Y. Usachov, I. A. Nechaev, G. Poelchen, M. Guttler, E. E. Krasovskii, S. Schulz, A. Generalov, K. Kliemt, A. Kraiker, C.

- Krellner, K. Kummer, S. Danzenbacher, C. Laubschat, A. P. Weber, J. Sanchez-Barriga, E. V. Chulkov, A. F. Santander-Syro, T. Imai, K. Miyamoto, T. Okuda, and D. V. Vyalikh, *Phys. Rev. Lett.* **124**, 237202 (2020).
- [31] H. J. Zhao, H. Nakamura, R. Arras, C. Paillard, P. Chen, J. Gosteau, X. Li, Y. Yang, and L. Bellaiche, *Phys. Rev. Lett.* **125**, 216405 (2020).
- [32] W.-T. Wang, C. Wu, S. Tsay, M. Gau, I. Lo, H. Kao, D. Jang, J.-C. Chiang, M.-E. Lee, Y.-C. Chang *et al.*, *Appl. Phys. Lett.* **91**, 082110 (2007).
- [33] Y. Iwata, N. Koyano, and I. Shibuya, *J. Phys. Soc. Jpn.* **35**, 1269 (1973).
- [34] G. Kresse and J. Hafner, *Phys. Rev. B* **47**, 558 (1993).
- [35] G. Kresse and J. Furthmüller, *Comput. Mater. Sci.* **6**, 15 (1996).
- [36] G. Kresse and J. Hafner, *J. Phys.: Condens. Matter* **6**, 8245 (1994).
- [37] G. Kresse and D. Joubert, *Phys. Rev. B* **59**, 1758 (1999).
- [38] J. P. Perdew, A. Ruzsinszky, G. I. Csonka, O. A. Vydrov, G. E. Scuseria, L. A. Constantin, X. Zhou, and K. Burke, *Phys. Rev. Lett.* **100**, 136406 (2008).
- [39] J. Heyd, G. E. Scuseria, and M. Ernzerhof, *J. Chem. Phys.* **118**, 8207 (2003).
- [40] H. J. Monkhorst and J. D. Pack, *Phys. Rev. B* **13**, 5188 (1976).
- [41] A. Togo and I. Tanaka, *Scr. Mater.* **108**, 1 (2015).
- [42] H. J. Zhao, P. Chen, C. Paillard, R. Arras, Y.-W. Fang, X. Li, J. Gosteau, Y. Yang, and L. Bellaiche, *Phys. Rev. B* **102**, 041203(R) (2020).
- [43] G. F. Koster, J. O. Dimmock, and R. G. Wheeler, *Properties of the Thirty-two Point Groups*, Vol. 24 (MIT Press, Cambridge, MA, 1963).
- [44] M. I. Aroyo, J. M. Perez-Mato, C. Capillas, E. Kroumova, S. Ivantchev, G. Madariaga, A. Kirov, and H. Wondratschek, *Z. Kristallogr.* **221**, 15 (2006).
- [45] L. Elcoro, B. Bradlyn, Z. Wang, M. G. Vergniory, J. Cano, C. Felser, B. A. Bernevig, D. Orobengoa, G. Flor, and M. I. Aroyo, *J. Appl. Crystallogr.* **50**, 1457 (2017).
- [46] Y. Hinuma, G. Pizzi, Y. Kumagai, F. Oba, and I. Tanaka, *Comput. Mater. Sci.* **128**, 140 (2017).
- [47] H. T. Stokes and D. M. Hatch, *J. Appl. Crystallogr.* **38**, 237 (2005).
- [48] W. R. Inc., Mathematica, Version 13.1, Champaign, IL, 2022.
- [49] U. Herath, P. Tavadze, X. He, E. Bousquet, S. Singh, F. Muñoz, and A. H. Romero, *Comput. Phys. Commun.* **251**, 107080 (2020).
- [50] S. Curtarolo, W. Setyawan, G. L. Hart, M. Jahnatek, R. V. Chepulskii, R. H. Taylor, S. Wang, J. Xue, K. Yang, O. Levy *et al.*, *Comput. Mater. Sci.* **58**, 218 (2012).
- [51] A. Jain, S. P. Ong, G. Hautier, W. Chen, W. D. Richards, S. Dacek, S. Cholia, D. Gunter, D. Skinner, G. Ceder *et al.*, *APL Mater.* **1**, 011002 (2013).
- [52] See Supplemental Material at <http://link.aps.org/supplemental/10.1103/PhysRevMaterials.6.094602> for $k \cdot p$ models, comparison of different functionals, crystal structures, band structures, spin textures, and phonon dispersions of some selected materials, which also includes the Refs. [5,41,44,47,51].
- [53] S. Abrahams, L. Zyontz, J. Bernstein, J. Remeika, and A. Cooper, *J. Chem. Phys.* **75**, 5456 (1981).
- [54] J. Choisnet, A. Deschanvres, and B. Raveau, *J. Solid State Chem.* **4**, 209 (1972).
- [55] O. Reckeweg, J. C. Molstad, S. Levy, C. Hoch, and F. J. DiSalvo, *Z. Naturforsch. B* **63**, 513 (2008).
- [56] L. C. L. Y. Voon and M. Willatzen, *The kp Method: Electronic Properties of Semiconductors* (Springer, New York, 2009).
- [57] G. Landolt, S. V. Eremeev, O. E. Tereshchenko, S. Muff, B. Slomski, K. A. Kokh, M. Kobayashi, T. Schmitt, V. N. Strocov, J. Osterwalder *et al.*, *New J. Phys.* **15**, 085022 (2013).
- [58] D. Pasquier and O. V. Yazyev, *Phys. Rev. B* **105**, L081106 (2022).
- [59] V. V. Volobuev, P. S. Mandal, M. Galicka, O. Caha, J. Sánchez-Barriga, D. Di Sante, A. Varykhalov, A. Khlar, S. Picozzi, G. Bauer *et al.*, *Adv. Mater.* **29**, 1604185 (2017).
- [60] P. Bhumla, D. Gill, S. Sheoran, and S. Bhattacharya, *J. Phys. Chem. Lett.* **12**, 9539 (2021).
- [61] A. Skierkowski and J. A. Majewski, *Acta Phys. Pol. A* **112**, 455 (2007).
- [62] L. Tao and J. Wang, *J. Appl. Phys.* **120**, 234101 (2016).
- [63] L. Leppert, S. E. Reyes-Lillo, and J. B. Neaton, *J. Phys. Chem. Lett.* **7**, 3683 (2016).
- [64] M. A. U. Absor, H. Kotaka, F. Ishii, and M. Saito, *Phys. Rev. B* **94**, 115131 (2016).
- [65] S. Sheoran, M. Kumar, P. Bhumla, and S. Bhattacharya, *Mater. Adv.* **3**, 4170 (2022).
- [66] M. Anshory and M. A. U. Absor, *Phys. E (Amsterdam)* **124**, 114372 (2020).